Vortex ring impingement on a wall with a coaxial aperture

JiaCheng Hu and Sean D. Peterson*
Department of Mechanical and Mechatronics Engineering, University of Waterloo, Waterloo, Ontario, Canada N2L 3G1

(Received 22 January 2018; published 29 August 2018)

The interaction of a vortex ring impinging on a rigid wall with a coaxial aperture is examined experimentally with various aperture sizes and vortex ring Reynolds numbers. Flow visualization and particle image velocimetry are utilized to investigate the dynamics of the impact interaction. For large aperture-to–ring radius ratios, the vortex ring passes through the aperture relatively unabated, while for smaller ratios, the incoming ring can be partially or completely blocked. For cases where the vortex ring is slightly smaller than the aperture, the vortex ring passes through, but suffers a significant loss in energy because of the influence of the wall. For apertures smaller than the ring, the vortex ring–wall interaction is similar to the dynamics of a vortex ring impacting a full wall; that is, the vortex ring-induced boundary layer separates and rolls up into a secondary vortex ring. Flow through the aperture, however, causes the formation of a new vortex ring. A semianalytical model is introduced to predict the strength of the newly formed vortex ring for small aperture-to-ring radius cases.

DOI: 10.1103/PhysRevFluids.3.084701

I. INTRODUCTION

Vortex ring–wall interactions are of academic interest and practical relevance. The impact event is dynamically rich, owing to the interplay between the incoming vortex ring's vorticity and the induced boundary layer vorticity along the wall. In a typical orthogonal impact, the approaching ring induces flow near the wall, resulting in a boundary layer with vorticity of opposite sign to that of the incoming ring core [1]. The ring radius begins to expand as it nears the wall, while the induced boundary layer encounters an adverse pressure gradient for radial locations on the order of the incoming ring radius and beyond. The adverse pressure gradient results in ejection of the boundary layer vorticity, which then mates with incoming ring vorticity and causes the ring pair to rebound from the wall prior to breaking down [1,2]. Using circulation and enstrophy evolution observations, Chu *et al.* characterized the interaction as having three phases: free-traveling vortex ring, vortex stretching, and rebounding [3].

Orlandi and Verzicco [2] and Swearingen *et al.* [4] conducted full three-dimensional simulations on orthogonal impacts with a focus on the instability development of the secondary vortex ring formed from the induced boundary layer vorticity. Orlandi and Verzicco demonstrated that the vorticity of the secondary vortex ring is too weak to overcome the strain, thus making the ring less resistive to azimuthal perturbations [2]. Swearingen *et al.* further analyzed the instability using linear stability theory, revealing that the instability of the secondary vortex ring is amplified by the vortex stretching and tilting of the primary vortex ring's strain field [4].

Chu *et al.* [5] and Naguib and Koochesfahani [6] experimentally investigated pressure loading on the wall during the collision, with Chu *et al.* finding that the vortices produce both suction and pushing forces on the wall, which nearly cancel each other out [5], while Naguib and Koochesfahani

*peterson@mme.uwaterloo.ca

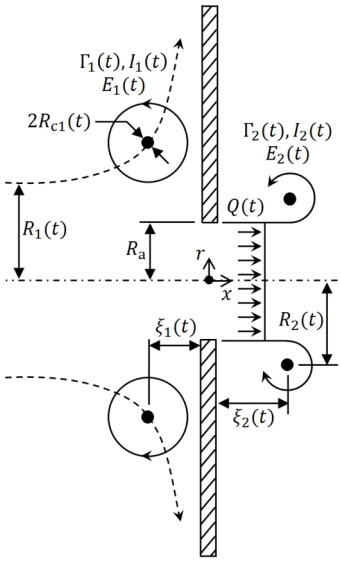

FIG. 1. Schematic of a vortex ring impinging on a rigid wall with a coaxially aligned aperture. The vortex ring on the left is the incoming vortex ring, while the vortex ring on the right is the postimpact vortex ring.

revealed that negative pressure sources are associated with vortex cores, while the positive pressure sources are associated with the stagnation region and the boundary layer formation [6]. Other vortex ring impact geometries and configurations have also been explored, including oblique impacts with flat rigid walls [7–10], collisions with spheres [11,12] and cylinders [13,14], and impingement upon porous screens [15–18].

Recently, Hu *et al.* explored the dynamics of a vortex ring impinging upon a flat wall with a coaxially aligned aperture [19]. After the impact, a vortex ring was observed propagating out the aperture. However, due the wall fixture, the region of impact was not optically clear, thus the details of the impact and postimpact vortex ring were not elucidated. Miloh and Shlien developed a potential flow model of a vortex ring interacting with a wall with a coaxial aperture and discovered a critical aperture–ring radius ratio that determines whether the vortex ring passes through or is blocked by the aperture [20]. This study necessarily neglected viscous effects, including vorticity roll-up at the aperture and induced boundary layers along the wall. Waelchli and Koochesfahani observed from their experimental study that the critical ratio is changed by the inclusion of viscosity, but no further details were provided and there was no mention of the formation of a second, postimpact vortex ring [21]. The current study aims to examine in more detail the interaction of a vortex ring with a coaxially aligned aperture, including the formation of the postimpact vortex ring observed by Hu *et al.* [19], as a function of ring-to–aperture radius ratio. Flow visualization and particle image velocimetry (PIV) are employed to elucidate the flow field, and a semianalytical model is developed to predict the strength of the postimpact vortex ring from details of the initial preimpact ring.

This article is organized as follows. The experimental setup is described in Sec. II. Experimental results and discussion are presented in Sec. IV. The semianalytical model is introduced and compared with experimental results in Sec. V. Section VI summarizes the work.

II. PROBLEM DEFINITION AND EXPERIMENTAL SETUP

Herein we explore the problem of a vortex ring impinging on a rigid wall with a coaxially aligned aperture in an otherwise quiescent fluid, as shown in Fig. 1. In this figure, the vortex ring on the left is the incoming vortex ring, while the one on the right is the postimpact vortex, which is generated during the collision.

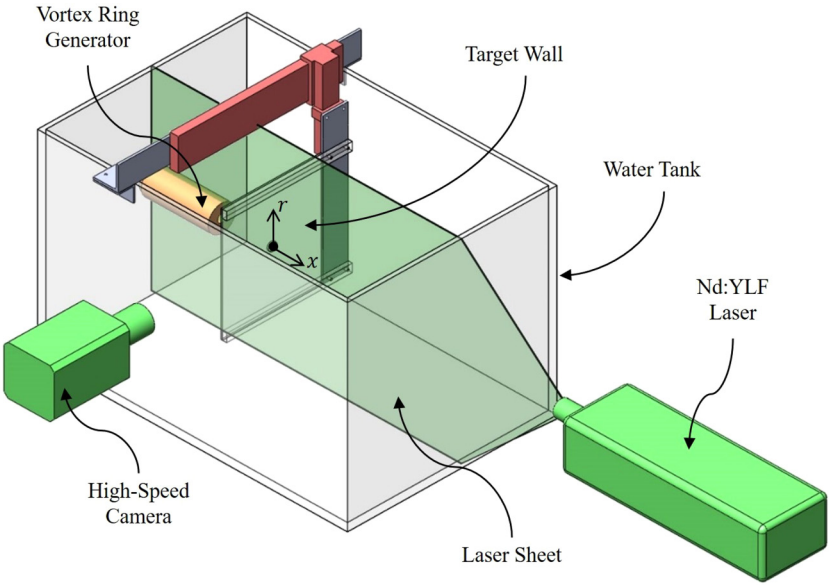

FIG. 2. Experimental setup.

A cylindrical coordinate system (r, x) is defined at the center of the aperture, as shown in Fig. 1, wherein r is the radial coordinate and x is the azimuthal coordinate, which is orthogonal to the aperture plane and pointing away from the incoming vortex ring. Properties associated with the incoming vortex ring are indicated with the subscript 1, while properties of the postimpact vortex ring behind the aperture are identified with the subscript 2. Each vortex ring is characterized by its radius R, core radius R_c, circulation Γ, impulse I, and energy E. The distance of a given ring from the wall is indicated by ξ. The vortex ring-induced flow across the aperture has a volumetric flow rate of Q and the aperture has a radius of R_a.

A. Experiment setup

The vortex ring–wall interaction is explored experimentally using a custom vortex ring facility shown in Fig. 2. The working fluid is water, which is contained in an acrylic tank with a wall thickness of 12.7 mm and interior dimensions of $914 \times 610 \times 610$ mm^3. The target wall is a 4.5-mm-thick Lexan sheet (SABIC Innovative Plastics) with dimensions 356×305 mm^2. Support bars are located at the top and bottom of the plate along the back side. The target wall is suspended on an L-bracket bridge that is placed across the width of the tank and is located at 98.9 ± 1.0 mm away from the vortex ring generator outlet. The target wall is removable to accommodate plates with different aperture sizes. To coaxially align the aperture with the impinging vortex ring, a cylinder is employed to extend the nozzle to the aperture for the positioning of the target wall. However, the alignment is conducted before water filling for better physical and visual access. Hence, the misalignment introduced by the filling process cannot be accounted for by the alignment process.

The vortex ring generator is a piston-cylinder configuration with a (25.4 ± 0.05)-mm-diam sharp-edged orifice outlet. The piston is located in a primary cylinder that has a diameter of 101.6 ± 0.05 mm. The piston is powered by a 1-hp dc motor (Boston Gear PM9100ATF-1) through a chain drive and a lead screw. The piston is controlled using a custom National Instruments (NI) LabVIEW VI through a NI DAQ PCIe-6323 card and a servo motor controller (Electro-Craft DC-35L). Image recording is triggered by the software 1 s before generator actuation in order to verify the quasistatic fluid assumption.

The fluid velocity field in a vertical plane passing through the vortex ring (and aperture) axis is measured via particle image velocimetry (PIV) produced by LaVision GmbH. The water is seeded

with silver-coated hollow glass particles (Potters Industries) with an average diameter of 13 μm and density 1.6 g/cm^3. The light source is a 20-mJ/pulse Nd:YLF laser (Photonics Industries DM20-527D/R). Images are recorded with a Photron FASTCAM SA4 (500K-M1) high-speed camera at full resolution (1024 $\times$ 1024 pixels) with frequencies of 100, 200, and 240 Hz for low-Reynolds-number PIV, high-Reynolds-number PIV, and flow visualization experiments, respectively. The field of view of the camera is 146 $\times$ 146 mm^2. The PIV recordings are postprocessed using a multipass interrogation scheme in DaVis 8.1.6 with a final interrogation window size of 32 $\times$ 32 pixels with 50% overlap. For the flow visualization studies, fluorescent dye is formulated by mixing water and fluorescent sodium salt (Sigma-Aldrich F6377).

B. Postprocessing of PIV vector fields

The azimuthal vorticity field ω_θ is computed from the velocity vector field at each time instant by Eq. (1) using a fourth-order central difference scheme [22,23], where u and v denote the x and r velocity components, respectively,

$$\omega_\theta = \frac{\partial v}{\partial x} - \frac{\partial u}{\partial r}. \tag{1}$$

Vortices are identified using the λ_2 criterion [23,24], which is computed using a least-squares differentiation scheme [23] with a threshold of $\lambda_2 < -5$. The selected threshold is small in comparison with the maximum value in the vortex ring core, thus enabling core identification throughout the interaction, but is sufficiently high to eliminate the background noise.

The positions of the vortex ring cores in the measurement plane are identified by the centers of their vorticity patches, while the core radii are estimated by fitting the vorticity patches to Gaussian distributions and computing a distances of one standard deviation from each peak [25,26]. The circulation, impulse, and energy of each vortex ring, assuming them to be axisymmetric, are computed as

$$\Gamma = \int_{\mathrm{A}} \omega_\theta \, dA, \tag{2a}$$

$$I = \pi\rho \int_{\mathrm{A}} \omega_\theta r^2 \, dA, \tag{2b}$$

$$E = \pi\rho \int_{\mathrm{A}} \omega_\theta \Psi \, dA, \tag{2c}$$

where ρ is the fluid density, dA is a unit area element, and Ψ is Stokes's stream function, which is obtained by multiplying the traditional stream function ψ by r [27]. The integrals in Eq. (2) are numerically approximated using the trapezoid rule. The stream function ψ is acquired by solving Poisson's equation with ω_θ as the source term [23],

$$\frac{\partial^2 \psi}{\partial x^2} + \frac{\partial^2 \psi}{\partial r^2} = \omega_\theta. \tag{3}$$

To compute ψ, Eq. (3) is discretized using a five-point second-order differencing scheme with $\psi = 0$ set as the boundary conditions in the far field and along the wall. All vortex ring properties are estimated as the average of the values computed for the top and bottom vortex cores in the planar slice through the ring.

Accurately estimating the volumetric flow rate through the aperture Q from the PIV data is hindered by imprecision in locating the aperture boundaries and the relatively small number of vectors spanning it. To mitigate these issues, a multistep process is employed to estimate Q. First, the center of the aperture is determined by locating its edges in the two-dimensional PIV images. This provides the location of the coordinate system defined in Fig. 2 in the experimental data. The velocity through the aperture is assumed to be axisymmetric. The radial velocity profile in the aperture is estimated by first averaging the velocity in two planes on either side of the wall, $\tilde{u}(r, 0, t) \approx$

TABLE I. Experimental parameters and uncertainties for the low-Reynolds-number cases (Re ≈ 1850).

Parameter	No aperture	Small aperture	Medium aperture	Large aperture
R_a (mm)		6.26 ± 0.05	12.78 ± 0.05	19.35 ± 0.05
h (mm)		2.59 ± 0.54	1.00 ± 0.88	1.36 ± 0.60
R_1^i (mm)	14.08 ± 0.58	14.13 ± 0.38	14.00 ± 0.26	14.05 ± 0.51
R_{c1}^i (mm)	2.82 ± 0.38	2.78 ± 0.15	2.88 ± 0.15	2.79 ± 0.16
Γ_1^i (mm^2/s)	1954.62 ± 105.00	1785.65 ± 39.96	1854.35 ± 50.49	1929.77 ± 61.26
I_1^i (μNs)	1222.73 ± 99.97	1126.66 ± 49.63	1162.13 ± 41.21	1208.20 ± 96.97
E_1^i (μJ)	56.90 ± 6.62	48.85 ± 2.63	51.24 ± 2.44	56.34 ± 4.40

$[u(r, x^-, t) + u(r, x^+, t)]/2$, where x^- and x^+ denote planes located immediately upstream and immediately downstream of the wall, respectively. Finally, since the PIV measurement plane contains two radial velocity profiles (one above the hole centerline and one below; see Fig. 2), these two profiles are also averaged to give $\tilde{u}^*(r, 0, t)$. The volumetric flow rate is finally obtained by integrating $\tilde{u}^*(r, 0, t)$ from $r = 0$ to the end of the field of view

$$Q(t) \approx 2\pi \int_0^\infty \tilde{u}^*(r, 0, t) r \, dr. \tag{4}$$

C. Experimental parameters

To examine the effects of varying the Reynolds number (defined as $\mathrm{Re} = \Gamma_1^i/\nu$, where ν is the kinematic viscosity and the superscript i denotes vortex ring properties measured when the ring is approximately three ring radii from the wall) and aperture-to–ring radius ratio R_a/R_1^i on the interaction process, a total of six different aperture scenarios are examined. Furthermore, PIV results of the collision with a solid wall are obtained as well to serve as a baseline. Specifically, we consider two Reynolds numbers, three aperture radii, and a solid wall case, as summarized in Tables I and II. We note that the variable h denotes the offset between the vortex ring centerline and the aperture centerline, which is a result of imperfections in the calibration process.

Each experiment is repeated five times and the results are averaged. The uncertainty in each parameter is estimated as the standard deviation of the measurements across the five repeated trials. The Reynolds number for the low- and high-Re cases are approximately 1850 and 4600, respectively, with some variability from experiment to experiment, as evidenced by the uncertainty in Γ in Tables I and II. All postprocessed data are filtered using a tenth-order low-pass Bessel filter with the cutoff frequency at 10% of the PIV sampling Nyquist frequency. We note that the low-Reynolds-number

TABLE II. Experimental parameters and uncertainties for the high-Reynolds-number cases (Re ≈ 4600).

Parameters	No aperture	Small aperture	Medium aperture	Large aperture
R_a (mm)		6.26 ± 0.05	12.78 ± 0.05	19.35 ± 0.05
h (mm)		2.87 ± 0.22	2.44 ± 0.30	0.40 ± 0.34
R_1^i (mm)	16.71 ± 0.55	16.57 ± 0.42	16.66 ± 0.37	16.73 ± 0.21
R_{c1}^i (mm)	2.94 ± 0.46	2.93 ± 0.22	2.83 ± 0.22	2.79 ± 0.09
Γ_1^i (mm^2/s)	4525.87 ± 224.91	4743.75 ± 146.51	4432.89 ± 214.64	4545.33 ± 128.30
I_1^i (μNs)	3983.94 ± 220.31	4152.82 ± 138.08	3902.71 ± 147.11	4020.49 ± 112.63
E_1^i (μJ)	390.42 ± 22.42	430.37 ± 24.51	378.38 ± 19.04	398.01 ± 23.46

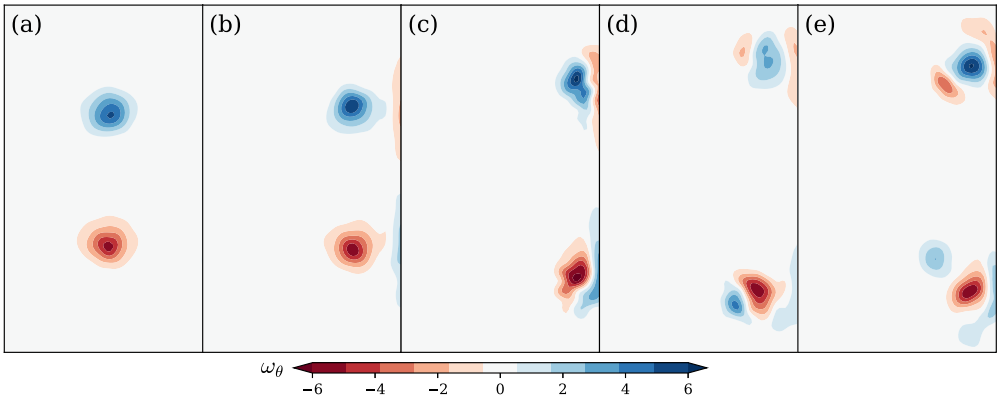

FIG. 3. Vorticity evolution of the high-Reynolds-number full wall collision scenario, increasing in time from (a) $t \approx 15$ to (e) $t \approx 27$ at an interval of $t \approx 3$. The wall is immediately to the right of each frame.

vortex rings are generated by applying a shorter stoke length to the piston, which leads to premature formation, resulting in smaller ring radii [28].

The experimental results are nondimensionalized using the initial ring radius R_1^{i} as the length scale, $(R_1^{\mathrm{i}})^2/\Gamma_1^{\mathrm{i}}$ as the timescale, and $\rho(R_1^{\mathrm{i}})^3$ as the mass scale, where ρ is assumed to be 1000 kg/m^3. For the remainder of the article, all variables shown are dimensionless unless otherwise noted. Finally, in the following sections, $t = 0$ corresponds to 1 s after the piston actuation begins, which is when data collection (image capture) commences.

III. RESULTS OF SOLID WALL COLLISION

The following section briefly reports on the PIV investigation of a vortex ring colliding with a solid wall without any aperture, in order to facilitate a baseline for the aperture cases. Furthermore, despite it being a well studied experimental problem, the complete evolution of the impinging vortex ring's integrated properties during the collision is rarely reported in the literature, which the results presented attempt to address.

The vorticity evolution of a vortex ring colliding with a flat wall is shown in Fig. 3. Before the collision, the vortex ring's central jet hits the wall and gets redirected outward, which produces a boundary layer in the process, as shown on the right side of Fig. 3(b). Upon collision, the impinging vortex ring expands radially. As a result of the vortex stretching, vorticity is concentrated within the vortex core, as illustrated by the higher peak vorticity and smaller core size of the primary vortex ring in Fig. 3. At the same time, the induced boundary layers begin to separate due to the adverse pressure gradient outboard of the ring induced by the proximity of the low-pressure vortex cores. In Fig. 3(d), the coupled interaction between the primary and secondary vortex rings leads them to rebound from the wall. Finally, the formation of a tertiary vortex ring is evident from the continuous production and separation of the boundary layers in Fig. 3(e). Overall, the qualitative description of the event is in excellent agreement with the literature [1,9].

The quantitative description of the vortex ring collision with a solid wall is presented in Fig. 4. The positions of the impinging vortex ring ξ_1, as shown in Fig. 4(a), demonstrate that the low-Reynolds-number scenario experiences a stronger deceleration due to greater viscous effects. Vortex rebound occurs in both cases as illustrated by the postcollision dip in ξ_1 at $t \approx 24$ and $t \approx 25.7$ for high and low Reynolds numbers, respectively. The radius of the impinging vortex ring R_1 expands to the same for the two Reynolds numbers, with the low-Reynolds-number case slightly delayed due to its aggressive deceleration during its approach [see Fig. 4(b)]. Regarding the ring's circulation evolution Γ_1 in Fig. 4(c), the low Reynolds number experiences a stronger loss both before and during the collision, again due to stronger viscous effects. Note that the circulation loss due to the

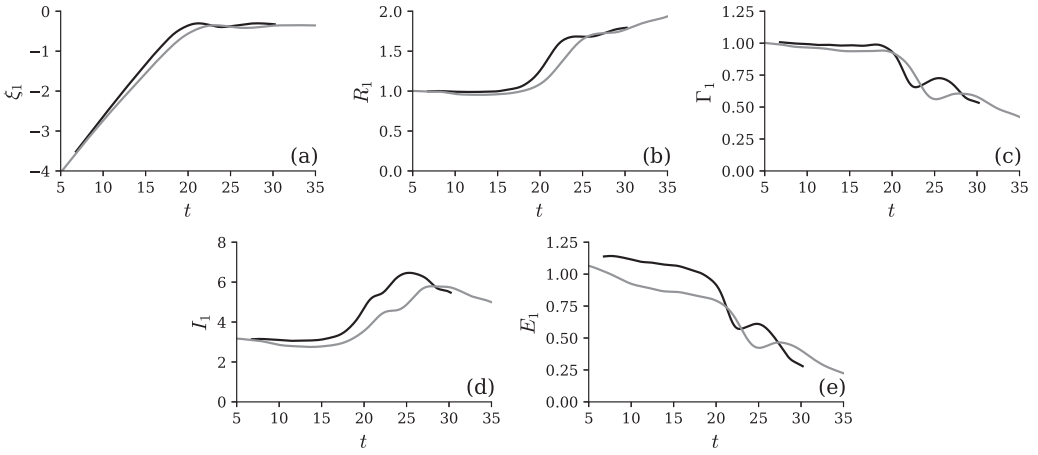

FIG. 4. Time series of the primary vortex ring during a full wall collision at Re ≈ 4600 (black line) and Re ≈ 1850 (gray line): (a) distance to the wall, (b) ring radius, (c) circulation, (d) impulse, and (e) energy.

wall interaction temporarily halts in both cases ($t \approx 24$ and $t \approx 25.7$ for high and low Reynolds numbers, respectively). This is a result of the rebounding action that brings the vortex core away from the wall, which reduces the rate of circulation loss to the wall. This was also observed in the numerical studies by Swearingen *et al.* [4] and Cheng *et al.* [29], though we also notice a slight dip in the circulation in our results, likely due to wall masking during the PIV processing. The impulse of the impinging vortex ring I_1 experiences an overall increase during the collision due to its radial expansion [11], in agreement with the prediction of a vortex ring thin core model ($I_1 \propto R_1^2$) [26]. The low-Reynolds-number case has an overall lower level of impulse, due to the increased vorticity cross annihilation between the vortex core and the induced boundary layer, which have opposite signs of vorticity. Finally, the kinetic energy E_1 of the impinging vortex ring decreases continuously, with a higher rate of loss upon impact. A temporary halt in energy loss is evident as it rebounds away from the wall, which can also be predicted from circulation evolution with the thin core model ($E_1 \propto \Gamma^2$) [26].

IV. RESULTS OF APERTURE COLLISION

A. Flow visualization

For a general description of the interaction of a vortex ring with a planar wall with a coaxial aperture, the flow visualization results for the high-Reynolds-number cases are presented in Fig. 5. Three distinctive behaviors are observed between the three aperture sizes. In Fig. 5(a), a laminar vortex ring approaches the small aperture. Upon impact in Fig. 5(b), the vortex core deforms into an elliptical shape, while a column of fluid is forced though the aperture. The front of the fluid column diverges outward as the jet begins to roll up. This is the same process as the vortex ring formation out of a piston-cylinder configuration described in Ref. [28]. A short time later in Fig. 5(c), the incoming vortex ring has merged with fluid ejected from the induced boundary layer along the wall to form a pair of conjoined rings; these appear as two mushroom-shaped dipoles in Fig. 5(c). This ejection and interaction process is very reminiscent of the interaction of a vortex ring impacting a solid wall (see, for example, [1]). Walker *et al.*, and our investigation in Sec. III, observed a tertiary vortex ring at a similar Reynolds number for a vortex ring–full wall impact [1], which is not observed here. We note that the near wall fluid is not marked, so the full picture is not necessarily elucidated. Also observed in Fig. 5(c) is a postimpact vortex ring formed from the fluid forced through the aperture.

For the medium-aperture case, shown in Figs. 5(d)–5(f), the core of the ring is also slightly deformed during the impact with the wall, and a much larger column of fluid is pushed though the

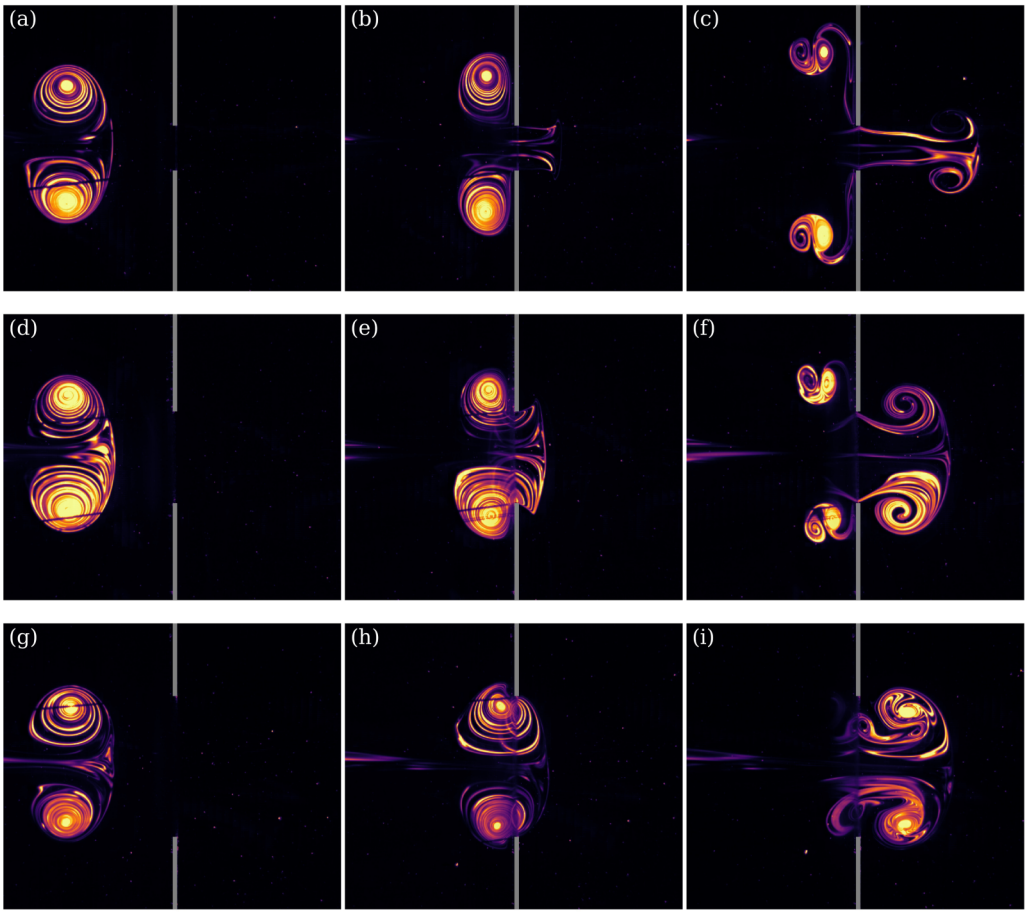

FIG. 5. Flow visualization snapshots for the high-Reynolds-number case for the (a)–(c) small-, (d)–(f) medium-, and (g)–(i) large-aperture cases. Snapshots at dimensional time $t = 3.33$, 3.75, and 4.08 s are shown in each column from left to right, respectively.

aperture. In this case, part of the incoming vortex ring core advects though the aperture, carrying some vorticity through, that joins with the vorticity formed at the aperture edge. In Fig. 5(f), we note that the interaction of the incoming vortex ring with the ejected wall boundary fluid (on the left side of the wall in the image) is similar to the small-aperture case. However, the size and trajectory of the conjoined rings are slightly smaller, implying that more energy is transferred to the postimpact vortex ring.

In the large-aperture case, shown in Figs. 5(g)–5(i), the aperture radius is greater than the ring radius; thus, the vortex core of the incoming ring does not interact appreciably with induced vorticity along the wall. In fact, the majority of the advecting vortex ring fluid appears to pass through the aperture, as shown in Fig. 5(i), though the aperture tip does causes significant disturbance to the vortex ring. As such, some energy is expected to be lost from the vortex ring in comparison with a free vortex ring traveling the same distance.

B. Vorticity fields

To gain quantitative insights into the vortex dynamics, we examine the vorticity fields of the interaction, again using the high-Reynolds-number case as the exemplar. The vorticity fields corresponding to approximately the same time points as in Fig. 5 are presented in Fig. 6.

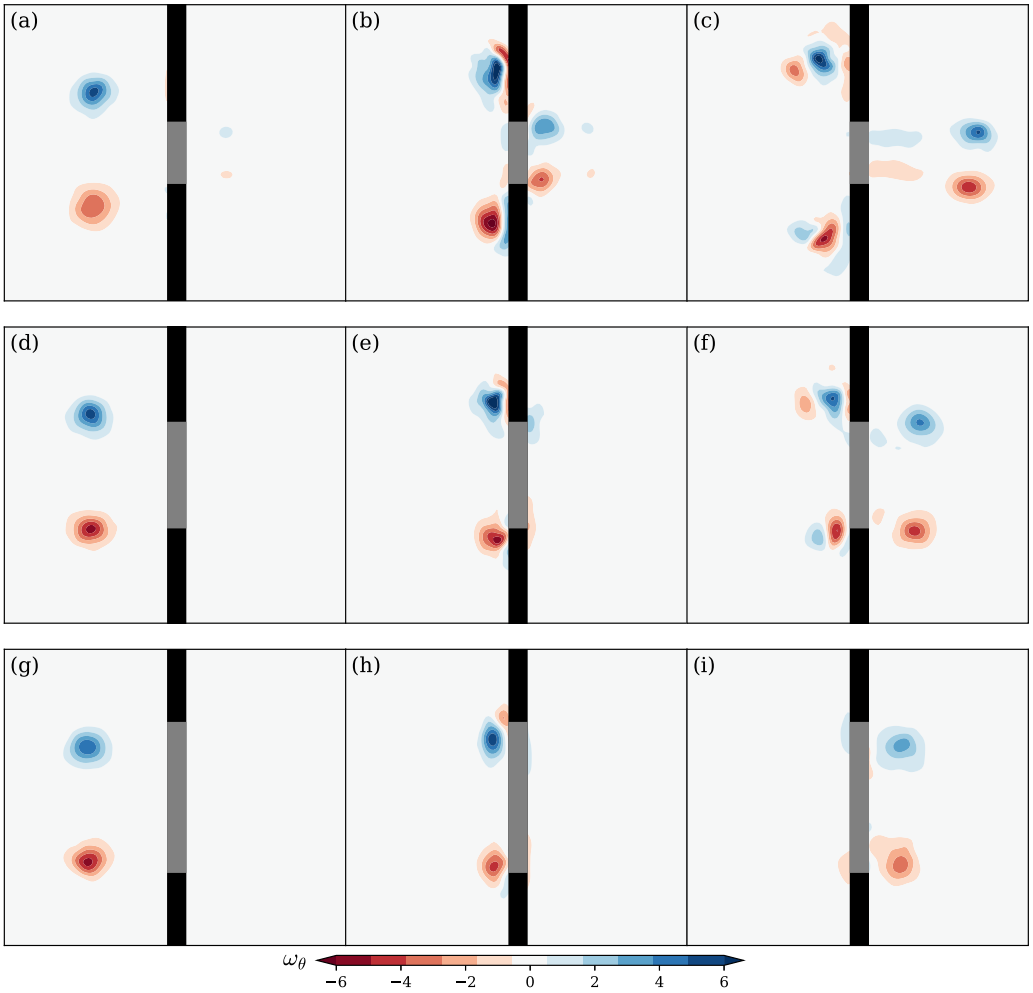

FIG. 6. Vorticity field snapshots of the high-Reynolds-number case for the (a)–(c) small-, (d)–(f) medium-, and (g)–(i) large-aperture cases. Snapshots of $t = 15$, 20, and 25 s are shown in each column from left to right, respectively. Gray and black areas are masked regions for the aperture and the wall, respectively.

We first note that there is a small vortex ring convecting out of the aperture for the small-aperture case [see Fig. 6(a)]. This is produced by a structural vibration during piston actuation and has very weak circulation in comparison to the preimpact vortex ring; as such, we presume its influence to be negligible.

The vorticity field of the small-aperture case is shown in Figs. 6(a)–6(c). Upon impact [Fig. 6(b)], the roll-up of boundary layer vorticity on the left side of the wall (facing the incoming vortex ring) can be seen. This is similar to the process of the collision on a wall without an aperture, as described in Sec. III, which suggests that the momentum or energy convected through the aperture is not sufficient to influence the unsteady boundary layer separation on the left of the plate. Hence, the losses of momentum or energy through advection (small-aperture case) is comparable to the losses through the no-slip condition at the wall (no-aperture case). Furthermore, vorticity associated with the newly formed postimpact vortex ring is observed to the right of the plate. The postimpact vortex ring induces weak opposite-signed vorticity near the aperture tip. This is in agreement with the piston-cylinder vortex ring formation process [28]. This patch of vorticity leads to postimpact vortex ring circulation loss due to opposite sign vorticity cancellation [28,30]. In Fig. 6(c), the postimpact

vortex ring, as well as the ring pair ejected from the left side of the wall (also seen in Fig. 5), is clearly visible. Also visible is the shear layer of the jet exiting the aperture caused by the initial preimpact vortex ring. There is a clear separation between the postimpact vortex ring and the trailing jet shear layer, indicating that the pinch-off has already occurred [31].

Upon impact of the incoming vortex ring with the medium aperture [Fig. 6(e)], we see that the induced vorticity on the left wall is weaker than in the no-aperture case. In Fig. 6(f), it is apparent that the ejected vortex ring pair (comprising the initial vortex ring and the induced boundary layer vorticity) has weaker strength and size in comparison to the no-aperture case. This suggests that some of the initial vortex ring's core vorticity passes through the hole, which brings along a significant portions of momentum or energy from the impinging vortex ring with it. The absence of trailing jet vorticity in Fig. 6(f) further suggests that the formation of the postimpact vortex ring is not terminated by the pinch-off process [31]; rather, formation terminates when the incoming vortex ring ceases feeding fluid through the aperture, resulting in submaximal vorticity in the postimpact ring. This change in behavior is likely a result of the increased radius of the postimpact vortex ring, which alters its limiting energy [31]. Finally, in the large-aperture case [Figs. 6(g)–6(i)], the approaching vortex ring simply passes though the aperture, though it does lose significant circulation in the process due to vorticity cancellation with the induced vorticity on the left side of the wall.

C. Temporal evolution of relevant properties

Time traces of relevant properties, including both the pre- and postimpact vortex ring properties and Q, are presented in Fig. 7. Recording of the incoming vortex ring properties commences once it fully enters the field of view and ends when the vortex detection algorithm, described in Sec. II B, is no longer able to adequately discern the ring vortices (that is, when the signal-to-noise ratio gets too low). On the other hand, recording of the postimpact vortex ring properties begins once it is fully formed, which is identified as the time when it reaches maximum circulation. We note that the dimensionless recording time is shorter for high-Reynolds-number cases since time is scaled by initial vortex ring properties. Also, data prior to the postimpact vortex ring formation is not computed, in large part, due to data loss through the PIV masking applied to the wall.

Time-history plots of the small-aperture cases are shown in the first column of Fig. 7. The incoming vortex ring behaves in a similar manner for both Reynolds numbers, though the low-Reynolds-number ring shows more rapid decay of initial circulation, as expected due to stronger viscous effects; as such, the ring's impulse and energy are lower. This observation is in agreement with the no-aperture cases in Sec. III. From Figs. 7(a) and 7(d) we observed a growth in radius and deceleration of the incoming ring as it approaches the wall. Circulation and energy drop significantly due to interaction with the aperture, including vorticity cancellation with the induced wall vorticity and loss through the aperture, as shown in Figs. 7(g) and 7(m). The vortex ring impulse increases [Fig. 7(j)] as the ring radius increases. Overall, the evolution of the impinging preimpact vortex ring does not deviate to any significant degree from the no-aperture cases, as described in Sec. III, which demonstrates that the loss through the aperture does not significantly influence the unsteady boundary layer separation process. Finally, the postimpact vortex ring also has smaller property values for the lower-Reynolds-number case, as shown by the dashed lines in Fig. 7.

Time traces for the medium-aperture cases are shown in the second column of Fig. 7. The trends are similar to the no- and small-aperture cases; however, there are three major differences. First, the incoming vortex is able to get closer to the wall and with less radial growth due to the larger opening. This results in minimal impulse growth during impact, which indicates that unsteady boundary layer separation process still occurs, but is significantly weakened. Second, the postimpact vortex ring has greater circulation and a larger radius due to the larger aperture. Finally, the formation times for the postimpact vortex ring, evidenced by the time point at the start of the dashed lines in the figure, are noticeably different between the two Reynolds numbers, unlike in the smaller-aperture case. This is an another indication that vortex ring pinch-off does not occur for the medium-aperture case; that is, the postimpact ring does not attain maximal circulation.

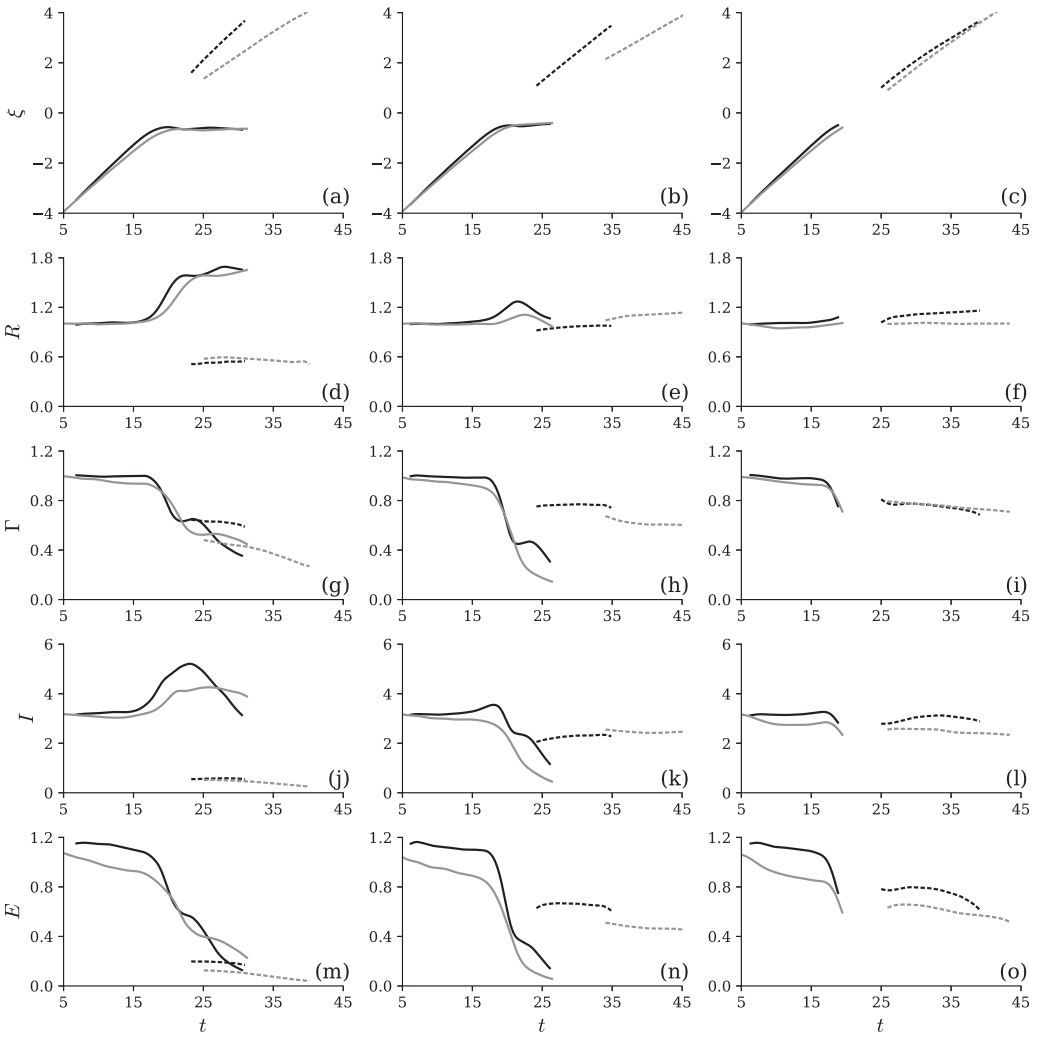

FIG. 7. Time series of vortex ring properties during the interactions. The small-, medium-, and large-aperture cases are presented in columns from left to right, respectively. The mean vortex ring x position, ring radius, circulation, impulse, and energy are organized into rows from top to bottom, respectively. Black and gray lines represent high- and low-Reynolds-number cases, respectively, while solid and dashed lines denote preimpact and postimpact vortex ring properties.

The larger-aperture case, shown in the third column of Fig. 7, tells a relatively simple story; the incoming vortex ring passes though the aperture and loses some of its energy in the process to cross-diffusive vorticity annihilation [30], as discussed in reference to Fig. 6. The unsteady boundary layer separation process no longer occurs.

D. Comparing pre- and postimpact rings

The properties of the postimpact vortex ring with respect to the properties of the incoming preimpact ring are compared in Fig. 8 for all cases considered. We remind the reader that the low- and high-Reynolds-number cases have slightly different aperture to ring radius ratios due to differences in the initial preimpact ring radii, as discussed in Sec. II C. The postimpact vortex ring properties are extracted when it is position at $\xi = 3$, which are normalized by the properties of a vortex ring at

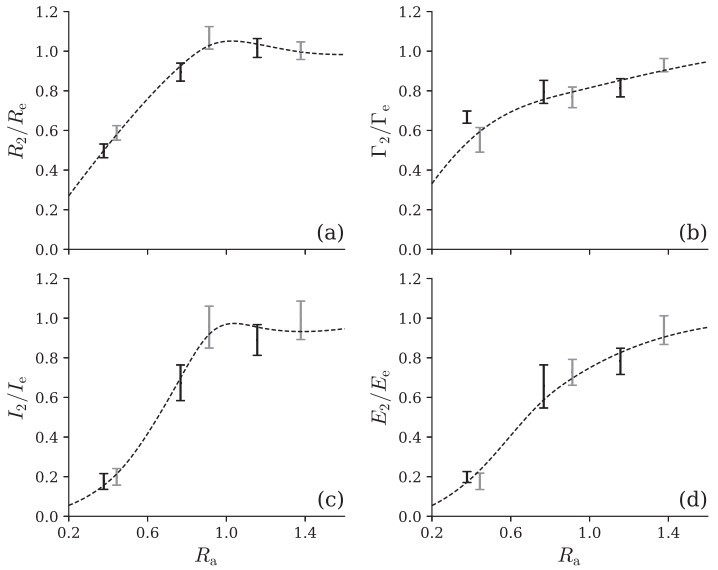

FIG. 8. Ratios of the post- to preimpact vortex ring properties versus aperture size for both Reynolds numbers: (a) ring radius R_2/R_e, (b) circulation Γ_2/Γ_e, (c) impulse I_2/I_e, and (d) energy E_2/E_e. High- and low-Reynolds-number cases are shown with black and gray symbols, respectively. Spline fit trend lines are also included.

$\xi = 3$ in the absence of an aperture, denoted by e. Properties in the absence of an aperture wall are linearly extrapolated using data from $t = 5$ to 15, to isolate the effects of the aperture without the influence of simple diffusion.

The variation of R_2/R_e with aperture size is shown in Fig. 8(a). The ratio first appears to increase linearly with the aperture size, likely due to the restriction on the postimpact vortex ring radius imposed by the aperture during formation [28]. When the aperture radius is nearly equal to the incoming ring (the medium-aperture case), the ratio appears to reach a maximum, which is greater than 1; that is, the outgoing postimpact ring is larger than the incoming ring. In this aperture size range, the interaction is transitioning from the formation of a new vortex ring at the hole to the incoming ring simply passing through the orifice. For larger aperture sizes, the ratio decreases back towards 1; obviously as $R_a \to \infty$, $R_2/R_1^i \to 1$.

For Γ_2/Γ_e, the circulation of the postimpact ring increases with aperture size; the circulation ratio should asymptote to a value slightly less than 1 as R_a increases towards infinity. The ratio of impulses shown in Fig. 8(c) follows the same general trends as the radius ratio, while the ring energy ratio in Fig. 8(d) is similar to the circulation ratio in behavior. We expect that I_2/I_e and E_2/E_e approach values near (but slightly below) 1 as $R_a \to \infty$. Overall, the behaviors appear to be relatively insensitive to Reynolds number in the range considered.

E. Vortex-induced flow through aperture

With regard to the volumetric flow rate through the aperture in Fig. 9, in all cases it increases as the preimpact vortex ring approaches the hole, reaching a maximum value around the time of impact. The flow rate then decays as the preimpact ring breaks down (or passes through the hole, in the case of the largest aperture radius). As expected, the total flow through the aperture increases with aperture size. We note that the large-aperture peak flow rate appears to be the same level as the medium-aperture case for low-Reynolds-number cases. This is likely a result of the smaller ring radius of the low-Reynolds-number cases, for which the vortex ring is able to pass through the medium aperture.

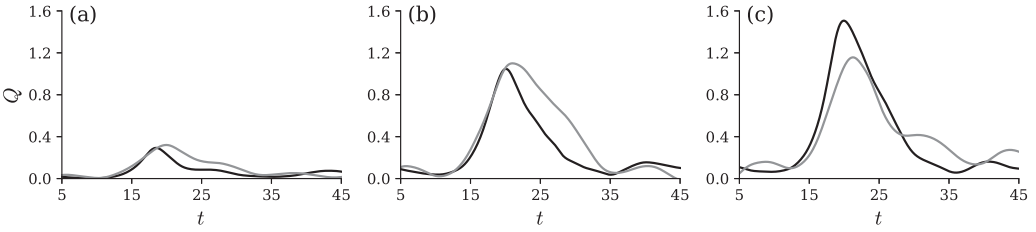

FIG. 9. Flow across the aperture induced by the impinging vortex ring for the (a) small-, (b) medium-, and (c) large-aperture cases; black and gray lines represent high- and low-Reynolds-number cases, respectively.

To further elucidate the vortex-induced flow through the aperture, the axial velocity profiles behind the aperture wall for the high-Reynolds-number cases are shown in Fig. 10. Due to wall masking, the profiles are taken at the $x = 0.22R_1^i$ plane. Hence, they are not necessarily the full representation of aperture flow profile. The first observation is that the small aperture has a noticeably different profile, where it approximates a free jet profile with the highest centerline velocity, indicating that the restrictive aperture significantly modified the induced flow. On the other hand, the medium- and large-aperture cases exhibit a drop in the centerline velocity, which resembles the vortex ring central jet profile, suggesting that the apertures do not completely disrupt the vortex-induced flow as the fluid passes through in these cases. The medium-aperture case has a higher velocity in the central region, again demonstrating that the aperture restriction increases the central region flow velocity.

Finally, we note that the misalignment of the initial vortex ring axis with that of the aperture is relatively large in comparison with the aperture radius in the small-aperture case. The jet profile of the small-aperture case is still symmetrical however, suggesting that the offset error does not have a major impact. This is expected since the aperture is still interacting with the vortex ring's central jet. In this case, the velocity variation is relatively small. We note, however, that the postimpact vortex ring formation is sensitive to small variations in the jet profile, which leads to a slightly angled postimpact ring trajectory.

F. Postimpact vortex ring formation for a small aperture

As we previously established with the experimental observations, the formation of the postimpact vortex ring is terminated by the pinch-off process, which was described by Gharib *et al.* for a

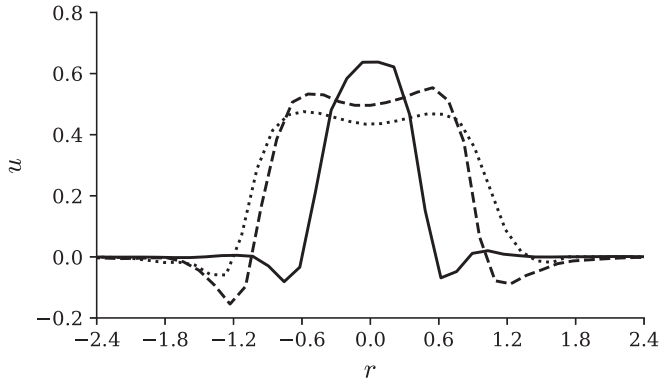

FIG. 10. Axial velocity profile behind the aperture ($x = 0.22R_1^i$) when the induced flow through the aperture reaches its peak for the high-Reynolds-number case. Solid, dashed, and dotted lines represent the small, medium, and large apertures, respectively.

piston-cylinder vortex generator [31]. Pinch-off refers to the separation of the leading vortex ring from its trailing jet, wherein the fluid ejected from an aperture is no longer able to roll up into the vortex ring, forming instead into a trailing jet behind the leading vortex ring. Gharib *et al.* explained this phenomenon using the Kelvin-Benjamin variational principle [32], which suggests that the pinch-off process occurs when the jet is unable to sustain the amount of the energy transfer required for a steady translating vortex ring with respect to its impulse-preserving isovortical perturbations [31,33–37].

The energy of a vortex ring can be normalized as

$$\alpha = \frac{E}{\sqrt{\rho I \Gamma^3}}. \tag{5}$$

The value of α decreases during formation until it reaches a limit, denoted by α_{lim}, and then the vortex ring pinches off from the jet and completes its formation. Gharib *et al.* experimentally discovered that the limiting normalized energy is $\alpha_{\text{lim}} \approx 0.33$ for a piston-cylinder configuration [31]. Additionally, the numerical study performed by Mohseni *et al.* demonstrated that the normalized energy is invariant if fluid ejection out of a piston-cylinder configuration has sufficiently long duration and sufficiently high Reynolds number [36], as well as producing an adequately thin shear layer [27].

It is unlikely that the above conditions are met for the current study, since the source of the fluid ejection is itself a vortex ring. Furthermore, Allen and Naitoh were able to produce a vortex ring with a much lower α_{lim} by using a variable radius orifice during formation [38]. With the post vortex ring properties computed using Eq. (2), we find that for both the Reynolds number cases in this study, the normalized energy is in the range of $\alpha_{\text{lim}} \approx 0.48 \pm 0.04$, which hints that the pinch-off process occurs much earlier during the formation in comparison to the piston-cylinder configuration.

V. ANALYTICAL MODEL

In this section, we develop an analytical model to predict the postimpact vortex ring properties based upon information about the incoming vortex ring for small R_1^{i}/R_a ratios. We treat the problem as primarily inviscid, neglecting the breakdown of the incoming vortex as it interacts with the wall. Vorticity production and diffusion from the aperture, which is the genesis of the postimpact vortex, is captured by adopting a slug model for vortex ring formation.

We begin with the potential flow model developed by Miloh and Shlien for a vortex ring approaching a wall with an aperture [20]. It has been recently employed by Hu *et al.* to model the pressure loading across an annular smart material energy harvester due to an approaching vortex ring [19]. The model assumes that the ring core radius is small in comparison with the ring radius. The dimensionless initial core radius of the experimentally generated ring is between $R_{\text{c1}}(0) = 0.17$ and 0.20 for the high- and low-Reynolds-number cases, respectively. Following Miloh and Shlien [20], the potential field in the $x < 0$ half space ϕ_+ contains three components

$$\phi_+(x, r) = \phi_{\text{v}}(x, r) + \phi_{\text{w}}(x, r) + \phi_{\text{a}}(x, r), \tag{6}$$

where $\phi_{\text{v}}(x, r)$ is the potential function for the incoming vortex ring, $\phi_{\text{w}}(x, r)$ is the mirror of the incoming vortex ring across the $x = 0$ plane required to model the wall, and $\phi_{\text{a}}(x, r)$ is a surface distribution of sinks of varying strength to model the aperture. The velocity field can be obtained by computing the gradient of the potential function. Full expressions for each term in Eq. (6) are presented in the Appendix.

The self-induction speed of a thin core vortex ring in an infinite medium, assuming a Gaussian distribution of vorticity in the core, is given by [25,26]

$$U_{\text{s}}(R_1, R_{\text{c1}}) = \frac{\Gamma_1}{4\pi R_1}\left[\ln\left(\frac{8R_1}{R_{\text{c1}}}\right) - 0.558\right]. \tag{7}$$

For the vortex core to satisfy continuity as the ring radius changes, the core must maintain a constant volume throughout the interaction. As such, the core radius at any time $R_{c1}(t)$ can be computed as

$$R_{c1}^2(t)R_1(t) = R_{c1}^2(0)R_1(0). \tag{8}$$

The total advection velocity of the incoming vortex ring (U_1, V_1) due to self-induction, the wall (image ring), and the aperture is

$$U_1(t) = \frac{d\xi}{dt} = U_a + U_w + U_s, \tag{9a}$$

$$V_1(t) = \frac{dR_1}{dt} = V_a + V_w, \tag{9b}$$

where (U_w, V_w) and (U_a, V_a) are the velocities at the vortex ring core due to the image ring (wall) and aperture, respectively. Full expressions for these velocity components are presented in the Appendix.

The volumetric flow rate across the aperture Q is computed as [20]

$$Q(\xi_1, R_1) = 2\pi \int_0^{R_a} \left.\frac{\partial \phi_+}{\partial x}\right|_{x=0} r\,dr = 2\Gamma_1\left\{R_a + \left[\left(R_1^2 + \xi_1^2 - R_a^2\right)^2 + 4\xi_1^2 R_a^2\right]^{1/4} \sin(\sigma/2)\right\}, \tag{10a}$$

where

$$\sigma(\xi_1, R_1) = \tan^{-1}\left(\frac{-2\xi_1 R_a}{R_1^2 + \xi_1^2 - R_a^2}\right). \tag{10b}$$

Inspection of Eq. (10) reveals that as $t \to \infty$, corresponding to $\xi_1 \to 0$ and $R_1 \to \infty$, the flow rate converges to a constant value of $Q = 2\Gamma_1 R_a$. This contradicts the observation in the present experiments, in which the volumetric flow rate initially increases before reaching a maximum and subsequently decreasing [see Figs. 7(m)–7(o)]. Furthermore, this implies that the vortex ring energy becomes unbounded, as seen from the equation for the energy of a vortex ring in an infinite medium [26]

$$E_1(R_1, R_{c1}) = \frac{1}{2}\Gamma_1^2 R_1\left[\ln\left(\frac{8R_1}{R_{c1}}\right) - 2.05\right]. \tag{11}$$

For fixed Γ_1, this expression is unbounded as $R_1 \to \infty$ regardless of the change in vortex ring core radius. In the real flow case (the experiments), breakdown of the incoming vortex ring contributes to the observed decay of the volumetric flow rate through the aperture, which is not captured in the inviscid model. Finally, this model assumes that the presence of the aperture wall does not significant alter the structure of the vortex core.

To resolve this issue with nonphysical model behavior in Q as $t \to \infty$, we propose a conservation of energy condition on the incoming vortex ring [assuming the expression for its energy (11) is not influenced by the wall or aperture]. Specifically, the total energy of the system E_s is set to be the initial incoming vortex ring energy, calculated from Eq. (11). This value remains invariant for the entire interaction under the potential flow assumptions, and thus

$$E_s = E_1(R_1(0), R_{c1}(0)) = \text{const}. \tag{12}$$

We estimate the rate of energy advected through the aperture, which forms the postimpact ring, using a slug flow model [28,31,33], to be

$$\frac{dE_2(t)}{dt} = \frac{Q^3(t)}{2\pi^2 R_a^4}. \tag{13}$$

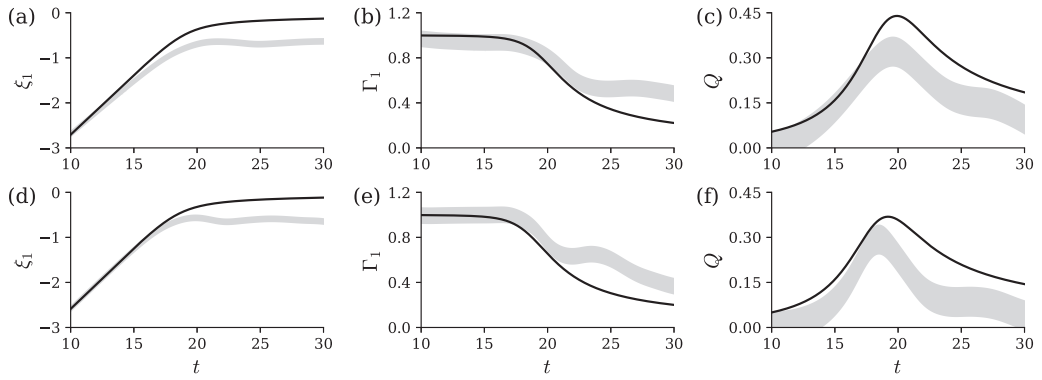

FIG. 11. Comparison of analytical and experimental results for the (a)–(c) low- and (d)–(f) high-Reynolds-number cases. The analytical results are displayed as black lines, while the experimental results with their 95% confidence intervals are represented with gray bands. The incoming vortex ring's (a) and (d) x position, (b) and (e) circulation, and (c) and (f) aperture flow rate are shown.

We note that the slug model assumes the radial velocity profile to be uniform. Hence, the incoming vortex ring energy at any time is

$$E_1 = E_s - E_2. \tag{14}$$

In order to maintain the constant total energy condition, that is, for the incoming vortex ring energy to decrease as a result of the interaction, the circulation of the ring must be allowed to vary in time. This in turn means that the advection speed of the vortex ring, as well as the aperture flow rate, will be time varying.

By combining Eqs. (6)–(14), the governing differential equations (9) and (13) can be solved to determine the system dynamics. The solution procedure is as follows.

(i) Integrate Eqs. (9) and (13) with respect to time using the FORTRAN ODEPACK LSODA algorithm to obtain the vortex ring position ξ_1 and energy loss E_2 through the aperture to the postinteraction vortex ring and its trailing jet.

(ii) Compute the vortex core size R_c using Eq. (8).

(iii) Compute the energy remaining within the impinging vortex ring E_1 assuming conservation of energy using Eq. (14).

(iv) Compute circulation Γ_1 using Eq. (11).

(v) Compute vortex core velocity U_1 or V_1 and rate of energy change dE_2/dt with Eqs. (9) and (13), respectively, and then return to the first step for the next time step.

The low-Reynolds-number case is simulated with initial conditions $\xi_1(0) = -5.0$, $R_{c1}(0) = 0.197$, and $R_a = 0.443$. The initial conditions of $\xi_1(0) = -5.0$, $R_{c1}(0) = 0.177$, and $R_a = 0.378$ are used for the high-Reynolds-number case. These values are extracted from the experimental measurements. Figure 11 compares the model prediction (black lines) with the experimental results, wherein the 95% confidence intervals for the experiments are shown as gray bands.

Figures 11(a) and 11(b) compare the predicted and measured incoming vortex ring x positions versus time for the low- and high-Reynolds-number cases, respectively. In both cases, initial agreement between the model and experiment is excellent, with the low-Reynolds-number results starting to diverge sooner due to viscosity. The model and experimental results for both the low- and high-Reynolds-number cases begin diverge around the time of the impact ($t \approx 20$). Additionally, the incoming vortex ring in the inviscid model propagates closer to the wall than in the experiments, likely due to the finite core size of the experimental ring (in comparison with the infinitesimal vortex core thickness assumed in the model). As previously stated, vortex ring breakdown is not captured in the model.

Figures 11(b) and 11(e) features the circulation comparison. Agreement between the model and the experiment is good until the boundary layer rolls up into the secondary vortex ring at $t \approx 20$. The aperture flow rate comparisons are shown in Figs. 11(c) and 11(f). Overall, the analytical model is able to forecast the trend and behavior well, although the model slightly overpredicts the flow magnitude. The overprediction is likely due to the lack of a viscous loss mechanism in the analytical model, as well as the nonuniformity of the aperture velocity profile. One possible modification to improve the model for future work is the inclusion of the postimpact vortex ring in the potential flow field model using the method proposed by Cho and Lee [39].

With the aperture flow rate prediction ability validated for the analytical model, we move to employing the Kelvin-Benjamin variational principle [32] to predict the postimpact vortex ring properties. As explained previously in Sec. IV F, the postimpact vortex ring formation is terminated when its normalized energy α reaches the limit $\alpha_{\text{lim}} \approx 0.48$ via the pinch-off process. The vortex ring properties will no longer change after pinch-off and thus the properties at this moment can be taken as the final postimpact vortex ring properties.

Again, we employ the slug model to estimate the properties of the flow across the aperture [31,33,35]. Assuming no loss across the aperture, the energy, momentum, and circulation of the jet are transferred to the postimpact vortex ring. Thus, utilizing the aperture flow rate Q obtained from the analytical solution, the energy of the postimpact vortex ring can be obtained using Eq. (13), while its impulse and circulation can be estimated with

$$\frac{dI_2(t)}{dt} = \frac{Q^2(t)}{\pi R_a^2}, \tag{15a}$$

$$\frac{d\Gamma_2(t)}{dt} = \frac{Q^2(t)}{2\pi^2 R_a^4}. \tag{15b}$$

All three properties at any time instance can be obtained by numerical integration and then the normalized energy α can be computed using Eq. (5). Once α reaches α_{lim}, the vortex ring is considered fully formed and its properties no longer change.

Using the experimentally obtained parameters $R_a = 0.378 \pm 0.009$ and $\alpha_{\text{lim}} = 0.48 \pm 0.04$, we obtain a post- to preimpact circulation ratio of $\Gamma_2/\Gamma_1 = 0.44 \pm 0.1$ for the high-Reynolds-number case. The experiment circulation ratio is $\Gamma_2/\Gamma_1 = 0.64 \pm 0.03$; we see that the model underpredicts the ratio, despite the overprediction of the aperture flow rate shown in Fig. 11(f). The discrepancy is partially due to the overprediction of the flow rate that causes the ring to reach the limiting energy faster, which leads to an earlier separation. The discrepancy is also potentially due to the use of a slug velocity profile; the numerical study by Rosenfeld *et al.* demonstrated that the velocity profile has a significant influence (up to 400%) on the ring formation values [34]. Furthermore, the roll-up of the incoming vortex ring keeps it near the aperture tip during the interaction, which could manipulate the formation process. This is similar to the situation of generating a train of vortex rings, where the leading vortex ring will alter the subsequent vortex ring formation [40,41]. The low-Reynolds-number case is not compared, since its high-viscosity effects further invalidate the slug model assumption for the flow though the aperture.

VI. CONCLUSION

This study examined the interaction of a thin core vortex ring impinging on a wall with a coaxially aligned aperture for two different incoming ring Reynolds numbers. Flow visualization and particle image velocimetry were employed to elucidate the impact mechanics for three aperture sizes, one smaller than the incoming ring, one with radius approximately equal to the ring radius, and one larger than it. In the small aperture-to–ring radius case ($R_a/R_1 \approx 0.41$), the interaction of the ring with the wall is similar to that of a ring impacting a solid wall. However, flow induced by the incoming ring passes through the aperture and rolls up into a second vortex ring, which eventually pinches off and advects away. The strength of the generated vortex ring scales with the Reynolds

number of the incoming ring, though its radius is only mildly influenced. When the aperture radius is approximately equal to the ring radius ($R_a/R_1 \approx 0.83$), the core partially passes through the aperture and merges with vorticity rolling up due to fluid passing through the hole. At larger aperture radius ($R_a/R_1 \approx 1.26$), the ring still passes through the hole, though it loses 35% of its initial energy in the process.

We introduced a model for predicting the postimpact vortex ring properties for the small-aperture case at high Reynolds numbers. The model combines a modified version of the potential flow solution introduced by Miloh and Shlien with a slug flow model for vortex ring formation at a sharp-edged orifice [20]. The original potential flow model predicts that flow through the aperture reaches and sustains a constant value as time goes to infinity, in contrast to the experimental observation. We overcome this by developing an energy conservation argument, which results in the incoming vortex ring circulation no longer being time invariant. The result is a model that reasonably captures the aperture flow rate and postimpact vortex ring properties observed in the experiments for the high-Reynolds-number case.

ACKNOWLEDGMENTS

This work was supported by the Natural Sciences and Engineering Research Council of Canada under Grant No. 2015-05778 and Alexander Graham Bell Canada Graduate Scholarship.

APPENDIX: INDUCED VELOCITIES FROM THE POTENTIAL FLOW MODEL

The full expressions of the terms in Eq. (6) are

$$\phi_v(x,r) = -\frac{\Gamma_1 R_1}{2}\int_0^\infty e^{k(\xi_1 - x)} J_0(kr) J_1(kR_1) dk, \tag{A1a}$$

$$\phi_w(x,r) = -\frac{\Gamma_1 R_1}{2}\int_0^\infty e^{k(\xi_1 + x)} J_0(kr) J_1(kR_1) dk, \tag{A1b}$$

$$\phi_a(x,r) = \frac{\Gamma_1 R_1}{\pi}\int_0^\infty \int_0^\infty \int_0^{R_a} e^{k\xi_1 + \lambda x} J_0(kr) J_1(kR_1)\cos(ks)\cos(\lambda s) ds\, d\lambda\, dk, \tag{A1c}$$

where $J_m(\cdot)$ denotes the Bessel function of the first kind of order m. The closed-form expressions for the wall-induced velocity components U_w and V_w are

$$U_w(\xi_1, R_1) = \frac{\Gamma_1 \eta}{4\pi R_1}[K(\eta^2) - E(\eta^2)], \tag{A2a}$$

$$V_w(\xi_1, R_1) = \frac{\Gamma_1 \eta \xi_1}{4\pi R_1^2}\left[2K(\eta^2) - \left(2 + R_1^2/\xi_1^2\right)E(\eta^2)\right], \tag{A2b}$$

where $K(\cdot)$ and $E(\cdot)$ are the complete elliptic integral of the first and second kinds, respectively, and η is

$$\eta(\xi_1, R_1) = \frac{R_1}{\sqrt{R_1^2 + \xi_1^2}}. \tag{A2c}$$

The aperture-induced velocity components U_a and V_a for the incoming vortex ring are

$$U_a(\xi_1, R_1) = \frac{\Gamma_1}{8\pi}\left\{8\sin\left(\frac{\sigma}{2}\right)\left[\left(R_1^2 + \xi_1^2 - R_a^2\right) + 4\xi_1^2 R_a^2\right]^{-1/4} - \frac{1}{\xi_1}\left[(1+\mu^2)\sin(\sigma) - \frac{1-\mu^2}{2}\sin(2\sigma)\right]\right.$$

$$+\frac{\mu}{\xi_1}\left[F\left(\sigma+\frac{\pi}{2},\eta^2\right)-F\left(\frac{\pi}{2},\eta^2\right)+E\left(\frac{\pi}{2},\eta^2\right)-E\left(\sigma+\frac{\pi}{2},\eta^2\right)\right]$$
$$-\frac{\mu^2}{\xi_1}\left[1+\frac{R_1^2}{\xi_1^2}\sin^2(\sigma)\right]^{\frac{1}{2}}\sin(\sigma)-\frac{1}{R_1}\ln\left[\frac{R_1}{\xi_1}\sin(\sigma)+\left(1+\frac{R_1^2}{\xi_1^2}\sin^2(\sigma)\right)^{1/2}\right]\Bigg\}, \tag{A3a}$$

$$V_a(\xi_1,R_1)=-\frac{\Gamma_1}{8\pi R_1}\Bigg\{8\left[R_1\cos\left(\frac{\sigma}{2}\right)+\xi_1\sin\left(\frac{\sigma}{2}\right)\right]\left[\left(R_1^2+\xi_1^2-R_a^2\right)^2+4\xi_1^2R_a^2\right]^{-1/4}$$
$$+\eta^2\left[\sin(\sigma)+\frac{\sin(2\sigma)}{2}\right]+2\mu\left[F\left(\sigma+\frac{\pi}{2},\eta^2\right)-F\left(\frac{\pi}{2},\eta^2\right)\right]$$
$$-\frac{1+\mu^2}{\mu}\left[E\left(\sigma+\frac{\pi}{2},\eta^2\right)-E\left(\frac{\pi}{2},\eta^2\right)\right]+\eta^2\left[1+\frac{R_1^2}{\xi_1^2}\sin^2(\sigma)\right]^{1/2}\sin(\sigma)\Bigg\}, \tag{A3b}$$

where $F(\cdot,\cdot)$ and $E(\cdot,\cdot)$ are the incomplete elliptic integrals of the first and second kinds, respectively, and μ is

$$\mu(\xi_1,R_1)=\frac{\xi_1}{\sqrt{R_1^2+\xi_1^2}}. \tag{A3c}$$

[1] J. D. A. Walker, C. R. Smith, A. W. Cerra, and T. L. Doligalski, The impact of a vortex ring on a wall, J. Fluid Mech. **181**, 99 (1987).

[2] P. Orlandi and R. Verzicco, Vortex rings impinging on walls: Axisymmetric and three-dimensional simulations, J. Fluid Mech. **256**, 615 (1993).

[3] C. C. Chu, C. T. Wang, and C. S. Hsieh, An experimental investigation of vortex motions near surfaces, Phys. Fluids A **5**, 662 (1993).

[4] J. D. Swearingen, J. D. Crouch, and R. A. Handler, Dynamics and stability of a vortex ring impacting a solid boundary, J. Fluid Mech. **297**, 1 (1995).

[5] C. C. Chu, C. T. Wang, and C. C. Chang, A vortex ring impinging on a solid plane surface—Vortex structure and surface force, Phys. Fluids **7**, 1391 (1995).

[6] A. M. Naguib and M. M. Koochesfahani, On wall-pressure sources associated with the unsteady separation in a vortex-ring/wall interaction, Phys. Fluids **16**, 2613 (2004).

[7] T. T. Lim, An experimental study of a vortex ring interacting with an inclined wall, Exp. Fluids **7**, 453 (1989).

[8] R. Verzicco and P. Orlandi, Normal and oblique collisions of a vortex ring with a wall, Meccanica **29**, 383 (1994).

[9] M. Cheng, J. Lou, and L. S. Luo, Numerical study of a vortex ring impacting a flat wall, J. Fluid Mech. **660**, 430 (2010).

[10] L. D. Couch and P. S. Krueger, Experimental investigation of vortex rings impinging on inclined surfaces, Exp. Fluids **51**, 1123 (2011).

[11] J. J. Allen, Y. Jouanne, and B. N. Shashikanth, Vortex interaction with a moving sphere, J. Fluid Mech. **587**, 337 (2007).

[12] P. J. S. A. Ferreira De Sousa, Three-dimensional instability on the interaction between a vortex and a stationary sphere, Theor. Comput. Fluid Dyn. **26**, 391 (2012).

[13] H. Ren, G. Zhang, and H. Guan, Three-dimensional numerical simulation of a vortex ring impinging on a circular cylinder, Fluid Dyn. Res. **47**, 025507 (2015).

[14] T. H. New and B. Zang, Head-on collisions of vortex rings upon round cylinders, J. Fluid Mech. **833**, 648 (2017).
[15] D. Adhikari and T. T. Lim, The impact of a vortex ring on a porous screen, Fluid Dyn. Res. **41**, 051404 (2009).
[16] J. T. Hrynuk, J. Van Luipen, and D. Bohl, Flow visualization of a vortex ring interaction with porous surfaces, Phys. Fluids **24**, 037103 (2012).
[17] C. Naaktgeboren, P. S. Krueger, and J. L. Lage, Interaction of a laminar vortex ring with a thin permeable screen, J. Fluid Mech. **707**, 260 (2012).
[18] M. Cheng, J. Lou, and T. T. Lim, A numerical study of a vortex ring impacting a permeable wall, Phys. Fluids **26**, 103602 (2014).
[19] J. Hu, Y. Cha, M. Porfiri, and S. D. Peterson, Energy harvesting from a vortex ring impinging on an annular ionic polymer metal composite, Smart Mater. Struct. **23**, 074014 (2014).
[20] T. Miloh and D. J. Shlien, Passage of a vortex ring through a circular aperture in an infinite-plane, Phys. Fluids **20**, 1219 (1977).
[21] S. Waelchli and M. M. Koochesfahani, *Fluids 2000 Conference and Exhibit, Denver* (American Institute of Aeronautics and Astronautics, Reston, 2000).
[22] A. Etebari and P. P. Vlachos, Improvements on the accuracy of derivative estimation from DPIV velocity measurements, Exp. Fluids **39**, 1040 (2005).
[23] M. Raffel, C. E. Willert, S. T. Wereley, and J. Kompenhans, *Particle Image Velocimetry: A Practical Guide*, 2nd ed. (Springer, Berlin, 2007).
[24] H. Vollmers, Detection of vortices and quantitative evaluation of their main parameters from experimental velocity data, Meas. Sci. Technol. **12**, 1199 (2001).
[25] P. G. Saffman, The velocity of viscous vortex rings, Stud. Appl. Math. **49**, 371 (1970).
[26] I. S. Sullivan, J. J. Niemela, R. E. Hershberger, D. Bolster, and R. J. Donnelly, Dynamics of thin vortex rings, J. Fluid Mech. **609**, 319 (2008).
[27] D. T. H. New and S. C. M. Yu, *Vortex Rings and Jets: Recent Developments in Near-Field Dynamics* (Springer, Singapore, 2015).
[28] N. Didden, On the formation of vortex rings: Rolling-up and production of circulation, J. Appl. Math. Phys. **30**, 101 (1979).
[29] M. Cheng, J. Lou, and T. T. Lim, Vortex ring with swirl: A numerical study, Phys. Fluids **22**, 097101 (2010).
[30] B. R. Morton, The generation and decay of vorticity, Geophys. Astrophys. Fluid Dyn. **28**, 277 (1984).
[31] M. Gharib, E. Rambod, and K. Shariff, A universal time scale for vortex ring formation, J. Fluid Mech. **360**, 121 (1998).
[32] T. B. Benjamin, The alliance of practical and analytical insights into the nonlinear problems of fluid mechanics, Appl. Methods Funct. Anal. Probl. Mech. **503**, 8 (1976).
[33] K. Mohseni and M. Gharib, A model for universal time scale of vortex ring formation, Phys. Fluids **10**, 2436 (1998).
[34] M. Rosenfeld, E. Rambod, and M. Gharib, Circulation and formation number of laminar vortex rings, J. Fluid Mech. **376**, 297 (1998).
[35] M. Shusser and M. Gharib, Energy and velocity of a forming vortex ring, Phys. Fluids **12**, 618 (2000).
[36] K. Mohseni, H. Ran, and T. Colonius, Numerical experiments on vortex ring formation, J. Fluid Mech. **430**, 267 (2001).
[37] C. O'Farrell and J. O. Dabiri, Pinch-off of non-axisymmetric vortex rings, J. Fluid Mech. **740**, 61 (2014).
[38] J. J. Allen and T. Naitoh, Experimental study of the production of vortex rings using a variable diameter orifice, Phys. Fluids **17**, 061701 (2005).
[39] C. H. Cho and D. J. Lee, Formulation for volume flowrate induced by vortex rings, through circular orifice of arbitrary section profile, Phys. Fluids **25**, 021702 (2013).
[40] T. T. Lim, A note on the leapfrogging between two coaxial vortex rings at low Reynolds numbers, Phys. Fluids **9**, 239 (1997).
[41] J. Satti and J. Peng, Leapfrogging of two thick-cored vortex rings, Fluid Dyn. Res. **45**, 035503 (2013).